Nano Energy 58 (2019) 47–56

Contents lists available at ScienceDirect

Nano Energy

journal homepage: www.elsevier.com/locate/nanoen

Full paper

A leaf-inspired photon management scheme using optically tuned bilayer nanoparticles for ultra-thin and highly efficient photovoltaic devices

Sonali Das[a], Mohammad Jobayer Hossain[b], Siu-Fung Leung[c,d], Anya Lenox[a,e], Yeonwoong Jung[a,f,g], Kristopher Davis[b,f], Jr-Hau He[c,d,*], Tania Roy[f,g,**]

[a] NanoScience Technology Center, University of Central Florida, Orlando, FL 32826, USA
[b] CREOL, The College of Optics and Photonics, University of Central Florida, Orlando, FL 32816, USA
[c] Computer, Electrical, and Mathematical Sciences and Engineering, King Abdullah University of Science and Technology, (KAUST), Thuwal 23955-6900, Saudi Arabia
[d] KAUST Solar Center, KAUST, Thuwal 23955-6900, Saudi Arabia
[e] Department of Chemistry, University of Central Florida, Orlando, FL 32816, USA
[f] Department of Materials Science and Engineering, University of Central Florida, Orlando, FL 32816, USA
[g] Department of Electrical and Computer Engineering, University of Central Florida, Orlando, FL 32816, USA

ARTICLE INFO

Keywords:
Leaf inspired
Hierarchical
Graphene Si Schottky junction solar cell
All dielectric
Whispering gallery resonator

ABSTRACT

We present a leaf-inspired biomimetic omnidirectional photon management scheme for ultrathin flexible graphene silicon Schottky junction solar cell. An all-dielectric approach comprising lossless spheroidal silica and titania nanoparticle bilayers is used for mimicking the two essential light trapping mechanisms of a leaf - focusing and waveguiding, and scattering. The ratio of the nanoparticle diameters of the two optically tuned layers plays a crucial role in confining the incident light through whispering gallery modes and subsequent forward scattering into the substrate *via* strong leaky channels. The scheme does not employ any nanostructuring of the silicon substrate, thereby preventing the optical gain from being offset by recombination losses, completely decoupling the optical and electrical performances of the device. The light-trapping scheme shows ultralow broadband reflection of only 10.3% and causes a 30% increase in efficiency compared to a bare graphene/silicon solar cell. An efficiency of ~9% is obtained for solar cell with 20 μm thick n-silicon absorber and doped bilayer graphene, resulting in highest (1.89) watt/gram utilization of silicon among all graphene/silicon solar cells. The light-trapping nanoparticle-embellished solar cell retains its characteristics for $> 10^3$ bending cycles for a bend radius as low as 3 mm, demonstrating its flexibility, durability and reliability.

1. Introduction

With the need for emerging photovoltaic cells to be fabricated on bendable supports and be capable of high speed roll-to-roll processing, silicon (Si)- the most widely used material in solar cells is gradually evolving towards a flexible future based on monocrystalline substrates [1–4]. For an ultrathin Si substrate, manipulation of the incoming light, in the form of collimation, scattering, focusing, and funneling, is needed which can lead to significant optical absorption enhancement in the active layer [5–7]. To realize an optimized photon management scheme for ultrathin Si substrate, nature has always been a source of inspiration for scientists [8]. Geometries found in insect eyes and wings have been studied extensively for harnessing solar energy [9]. Si surface has been engineered to mimic bio-inspired structural geometries like nanopillars, nanowires, nanodomes and nanocones for achieving suppressed reflection over a broad range of wavelengths and allowing more light to couple inside Si [8,10–17]. However, texturizing the Si substrate to enhance light-trapping will unavoidably increase the surface area, causing surface degradation by increased density of surface traps, increasing surface recombination and eventually decreasing the solar cell efficiency. Since the planar Si is highly reflective over the AM1.5G solar spectrum, it is imperative to use an effective light-trapping scheme devoid of Si structuring to decouple the optical and electrical domains.

This necessitates the quest to investigate the light manipulation methods present in nature. Specifically, the benefits offered by leaf surfaces for photon management and light harvesting remains relatively unexplored. Leaves have adapted themselves to meet the essential prerequisite of funneling light energy efficiently and channeling it to the

* Corresponding author at: Computer, Electrical, and Mathematical Sciences and Engineering, King Abdullah University of Science and Technology, (KAUST), Thuwal 23955-6900, Saudi Arabia.
** Corresponding author at: NanoScience Technology Center, University of Central Florida, Orlando, FL 32826, USA.
E-mail addresses: jrhau.he@kaust.edu.sa (J.-H. He), Tania.Roy@ucf.edu (T. Roy).

https://doi.org/10.1016/j.nanoen.2018.12.072
Received 19 November 2018; Received in revised form 22 December 2018; Accepted 22 December 2018
Available online 24 December 2018
2211-2855/ Published by Elsevier Ltd.

reaction centers to promote photosynthesis [18,19]. Leaves typically have hierarchical morphologies with optimized micro and nanostructures of various shapes and sizes which can efficiently control the amount of incident solar radiation to be captured and coupled into itself. The light trapping in the leaf is enabled by multiple cellular hierarchical layers with varying functionalities working with an optical synergy. While the upper part of the leaf focuses and guides the incident light into the leaf, the lower part with irregular shaped cells maximizes the scattering of the in-coupled light enhancing the light absorption. Depending on the large temporal and spatial variation of the incoming light on daily and annual basis, leaves have evolved to successfully couple light over wide angles of incidence making them possess omnidirectional characteristics.

Inspired by the light-harvesting phenomena in the leaf, a hierarchical bilayer light-trapping scheme when engineered properly can exactly replicate and mimic the functionalities of a leaf. The top layer can be a periodic arrangement of Whispering Gallery Mode (WGM) dielectric resonators which leads to the focusing and coupling of light between the spheres leading to a waveguide formation [20,21]. Dielectric resonators supporting WGM are generally characterized by their high quality factor (Q). But WGM resonators used for solar cell applications must have low Q, low frequency selectivity and strong incoupling for the absorber region [22]. The low Q of WGM resonators depends on the bending loss occurring due to the leakage of light which, in turn, depends on the nanoparticle environment [23,24]. Therefore, to achieve low-Q WGM resonators suitable for photovoltaic applications, it is essential to tune the environment of the WGM resonator allowing for sufficient leaky channels for the light to couple from the dielectric nanosphere to the underlying Si. Significant light absorption is obtained for photovoltaic absorber with periodic array of resonant spheres and spherical nanoshells due to strong whispering gallery modes [20,22,25]. But, discrete nature of each resonant mode makes it trivial to maintain the phase matching with the incident solar energy spectrum which is required for achieving a broadband absorption enhancement [5,26]. This opens up an opportunity to control the direction of the scattering. To achieve broadband absorption within Si, forward scattering needs to be enhanced with almost negligible back scattering. The bottom layer can therefore be designed to provide leaky channels for the light from the WGM resonators to the Si with optimum forward scattering into the absorber. Such a hierarchical biomimetic design would allow for the implementation of various light management functionalities so that the optical and electrical domains of the solar cell can be decoupled from each other, offering immense design flexibility and easy adaptability into any type of solar cell technologies.

In this paper, we demonstrate such a comprehensive novel leaf-inspired photon management scheme on the flexible and ultrathin graphene/Si Schottky junction solar cells. The application of graphene on Si solar cells has attracted much attention in recent years due to the ease and low cost of fabrication, concomitant with the lucrative properties of high electron mobility, transparency and mechanical flexibility of graphene as a transparent conducting electrode [27–35]. The bilayer light-trapping scheme consisting of a top layer of silica spheres and a bottom layer of titania spheres to mimic the exact light trapping phenomena found in leaves. Specifically, we have employed the Finite Difference Time Domain (FDTD) optical simulation to study the optimal geometry of the bilayer light trapping scheme and to analyze the light trapping mechanism. The size of the nanoparticles in each layer plays a crucial role and has been optimized for infiltrating the critical optical features of the leaf including focusing, waveguiding and scattering of light. The three unique properties offered by our leaf-inspired photon management scheme are: (1) it uses lossless all-dielectric approach, (2) it is free of recombination centers since it does not involve Si surface structuring, and (3) it offers broadband polarization-independent antireflection characteristics for light striking at normal and oblique angles of incidence. Such simple, hierarchical, low-cost light-trapping schemes are universal in nature, devoid of recombination losses and are potentially viable for any solar cell technology. The planar Si surface of the solar cell is passivated by a layer of aluminium oxide (Al_2O_3) and the graphene film is p-doped with gold chloride ($AuCl_3$). An optimal Si thickness coupled with the optimized light-trapping scheme leads to efficient photon harvesting. The *PCE* of a nanosphere-decorated 20 μm thick graphene/Si solar cell improves to 8.8%, which is 1.3 × higher than the pristine cell's *PCE* of 6.8%. Additionally, the photovoltaic characteristics of the laminated solar cell show negligible change after several bending cycles for bend radii as low as 3 mm. After 3×10^3 bending and straightening cycles, the biomimetic light trapping layer and the ultrathin solar cell retains its performance. The leaf-inspired dual-layer nanoparticle reported in this work demonstrates a simple, ultra-durable and omnidirectional light trapping scheme with proved performance on the ultra-thin Si solar cells which is of paramount importance in future development of photovoltaics.

2. Results and discussion

2.1. Optimization of the light trapping scheme

The key mechanisms behind the interaction of a leaf with light can be revealed by the structural components of the leaf [36,37]. The propagation of light through the leaves is governed primarily by focusing, funneling and scattering interactions. Fig. 1**a** shows a typical schematic of the leaf anatomy including the upper and lower epidermis, palisade *meso*phyll and spongy *meso*phyll cells. The upper epidermis is primarily thin and transparent and consists of lens-type cells capable of focusing light. This layer facilitates path length enhancement of the incident light increasing its probability to get absorbed and allows omnidirectional absorption. Elongated and densely packed palisade cells contain the largest proportion of chloroplasts supporting photosynthesis. This layer enables the penetration of sunlight deep inside the leaf and behaves as a waveguide to trap the light. The spongy *meso*phyll layer consists of irregular cells with large intercellular spaces filled with air. Due to the huge discontinuity between the absorbing material and the air-filled space, there arises a refractive index mismatch in the cellular interfaces. This helps in scattering light within the leaf for increasing its chance to get absorbed for photosynthesis. To mimic the optical behavior observed in the leaf, we have designed a unique light-trapping scheme for the graphene/Si solar cells. The schematic of the graphene/Si solar cell is shown in Fig. 1**b**. An interfacial oxide layer of Al_2O_3 is deposited on Si to passivate its surface by reducing the recombination centers and to improve the open circuit voltage (V_{oc}) [35,38,39]. Bilayer graphene is then transferred onto the Si substrate. Although bilayer graphene exhibits a lower transmittance of 95.3% compared to 97.6% transmittance by monolayer graphene, the sheet resistance of bilayer graphene is almost half of that of monolayer graphene, thus offering a tradeoff between their electrical and optical performances [40]. The light-trapping scheme as shown in the schematic consists of a bilayer configuration of densely packed hexagonal arrays of titania nanoparticles and silica nanoparticles. Fig. 1**c** shows the schematic of the light management mechanism in the proposed bilayer configuration. The size of the silica nanoparticles in the top layer must be greater than that of titania nanoparticles in the bottom layer to play a crucial role for guiding and propagating light in a manner similar to that observed in the leaf. The top silica layer plays a composite role of focusing and funneling of light, analogous to the upper epidermis and palisade *meso*phyll cells of the leaf. The particles in this layer have a circular symmetry and can sustain the whispering gallery modes. Light of a particular wavelength gets confined within the large sized particles by total internal reflection with increased number of round trips along the surface until it finds a strong leakage channel provided by the bottom layer. The bottom layer offers the role of scattering like the spongy *meso*phyll layer in the leaf. Smaller nanoparticles scatters optimum light in the forward direction into the underlying high indexed Si substrate through the transparent graphene

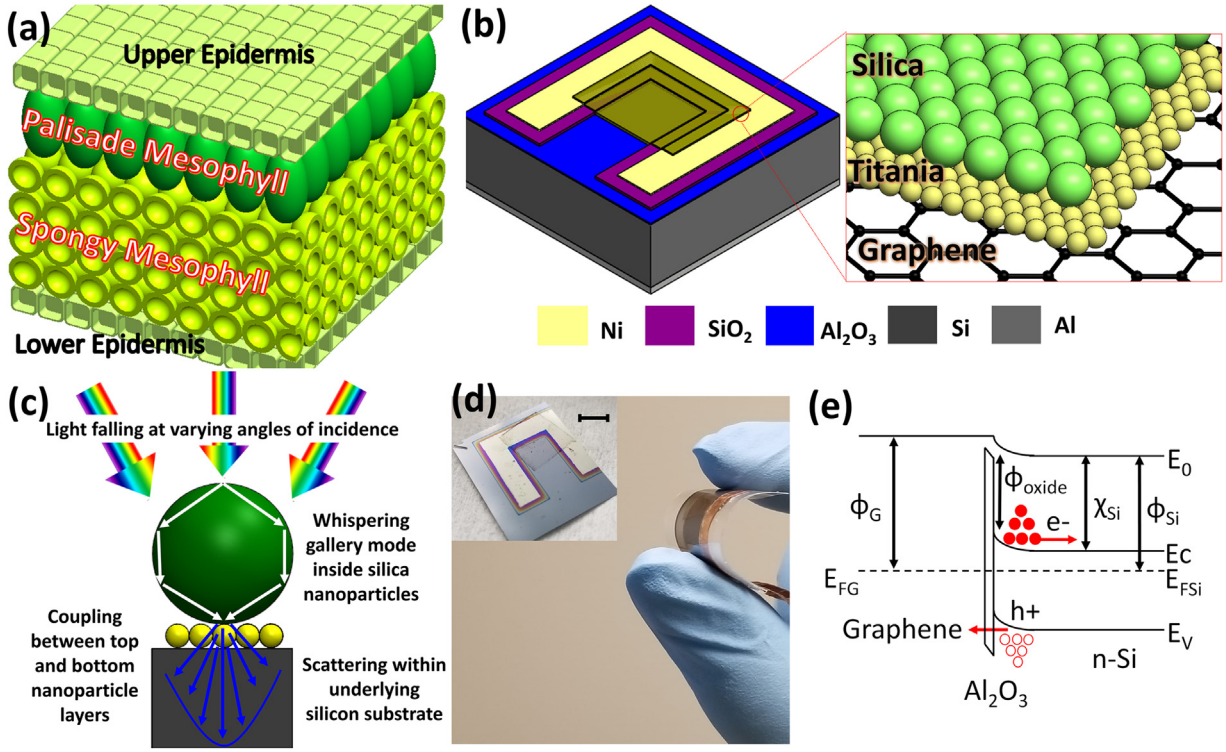

Fig. 1. Schematic of leaf-inspired graphene/Si solar cell with fabricated device and energy band diagram. (a) Schematic representation of leaf anatomy consisting of upper and lower epidermis, palisade *meso*phyll and spongy *meso*phyll tissues. (b) Schematic representation of the graphene/Si solar cell with the light-trapping scheme. The expanded region shows the bilayer configuration of hexagonal arrangement of silica/titania nanoparticles on graphene. (c) Schematic of the light management mechanism in the proposed bilayer light-trapping scheme with all-dielectric spheres. (d) Photograph of a flexible thin graphene/Si solar cell. Inset shows the optical image of a complete graphene/Si solar cell. Scale bar 0.5 cm. (e) Energy band diagram of the graphene/Si Schottky junction.

film with minimal back scattering. Fig. 1**d** shows the optical image of a representative ultra-thin flexible graphene/Si solar cell. Fig. 1**e** shows the energy band alignment at the doped graphene/Si interface under illumination with an Al_2O_3 passivation layer between graphene and Si. Graphene forms a Schottky barrier with n-Si because of the difference between the work function of graphene (ϕ_G) and that of Si (ϕ_{Si}). The photo-generated holes are collected by the graphene layer as they tunnel through the Al_2O_3 barrier. A high barrier height (ϕ_{oxide}) is desired for preventing the tunneling of electrons through the passivation layer. An optimal thickness of 5–30 Å of Al_2O_3 helps improve the photo-conversion efficiency (*PCE*) of the solar cell by allowing efficient hole tunneling and increasing V_{oc} by reducing carrier recombination [35,41,42]. In this work, 1 nm thick Al_2O_3 is deposited on the silicon surface by atomic layer deposition. In addition, the p-doping of graphene enhances the graphene/Si Schottky barrier, resulting in a higher V_{oc}. Simultaneously, doping graphene reduces the series resistance of the solar cell, thus improving the fill factor (*FF*).

Light management for ultrathin substrates has two major challenges: (a) optimizing a light trapping scheme for enhancing the optical absorption within physically thin substrates and (b) optimizing the physical thickness of the active layer to achieve a high *PCE*. To maximize photon harvesting and to minimize the optical reflectance, a synergistic association of the light-trapping scheme with the thickness of the underlying Si is required. We performed 3D full field electromagnetic simulations with Lumerical® FDTD Solutions to predict the optimal size of the nanoparticles in the light-trapping layer on an optimized thickness of the Si substrate. The objective is to obtain the minimum possible integrated reflectance for an optimized thickness of Si. To perform the optimization, we simulated the light-trapping scheme with varying *D:d* ratios, where *D* is the diameter of silica nanoparticles, and *d* is the diameter of the titania nanoparticles. We chose $d = 50$ nm, 100 nm and 200 nm for reasons that will be explained in the subsequent paragraphs. The parameter space for *d* is chosen to find an optimum size parameter of the titania nanoparticles in which simultaneous reduced back scattering and optimized forward scattering can be achieved. The *D:d* ratio was varied from 1 to 10 for each value of *d*, thus varying *D* from 50 nm to 2 μm. This range of values allows for the bilayer light trapping scheme to closely mimic the architecture of the leaf in which $D > d$ and facilitates an optimum combination to achieve minimum reflection losses for a Si substrate. The integrated reflectance (R_{int}) is calculated using the following equation:

$$R_{int} = \frac{\int_{\lambda=400\text{ nm}}^{1100\text{ nm}} R(\lambda)N_0(\lambda)d\lambda}{\int_{\lambda=400\text{ nm}}^{1100\text{ nm}} N_0(\lambda)d\lambda} \quad (1)$$

where $N_0(\lambda)$ is the number of photons for the incident AM1.5G solar spectrum and $R(\lambda)$ is the reflectance corresponding to wavelength λ. The integrated reflectance due to the incorporation of the light-trapping scheme on the graphene/Si substrate for a constant Si thickness of 20 μm has been plotted in Fig. 2**a**. The optimization has also been performed for lower thicknesses of the Si substrate (10 μm and 15 μm), as shown in Fig. S1**a–b** in Supporting Information. It is observed that for a ratio of *D:d* of 6 when $D = 600$ nm and $d = 100$ nm, R_{int} reaches a minimum value of ~7.32% for a 20 μm thick Si substrate. Fig. 2**b** shows the wavelength-dependent reflectance for a 20 μm thick Si substrate with and without the optimized light trapping structure. It is observed that the reflection is ultra-low over a wide range of wavelength, with significantly reduced reflectance for the solar cell embellished with the light-trapping structure compared to the bare one. The reflectance remains below 3% for the spectrum ranging from 540 to 740 nm resulting in the low integrated reflectance for the entire solar spectrum (400–1100 nm). This accounts for ~80% reduction in reflectance compared to a bare graphene/Si surface for the same thickness of Si. Further, based on this optimized pattern, wavelength integrated reflectance of graphene/Si substrates as a function of Si thickness is

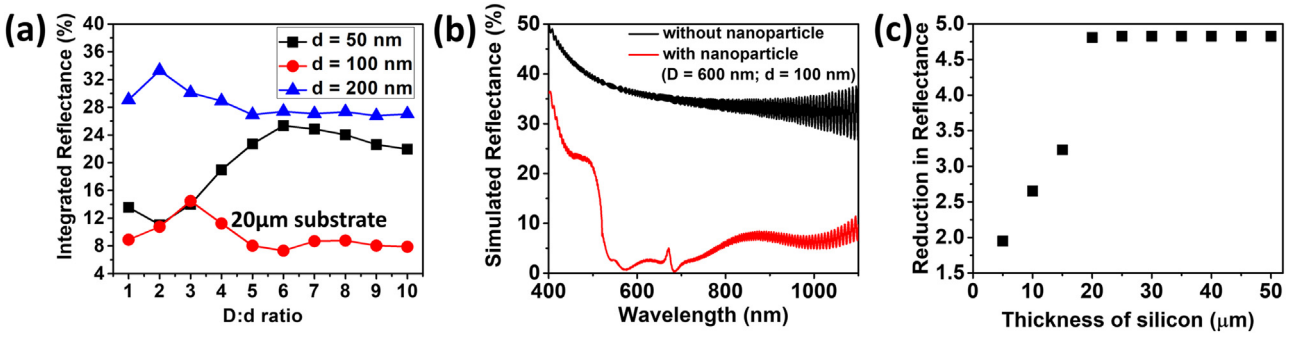

Fig. 2. Optimization of the light-trapping scheme. (a) Optimization of the diameter of the densely packed hexagonal arrays of titania nanoparticles and silica nanoparticles in the bilayer light trapping scheme for 20 μm thick Si substrate. D is the diameter of silica nanoparticles, and d is the diameter of the titania nanoparticles. (b) Wavelength-dependent reflectance of the optimized combination of the nanoparticles (D = 600 nm, d = 100 nm) in the light-trapping scheme. The optimized combination of nanoparticles (D = 600 nm, d = 100 nm) is obtained from Fig. 2a. (c) Reduction in integrated reflectance due to the optimized light-trapping structure (D = 600 nm, d = 100 nm) for varying thicknesses of Si substrate.

studied. Fig. 2**c** shows the reduction in reflectance as calculated by the ratio of R_{int} of bare graphene/Si to R_{int} of graphene/Si with the optimized light-trapping scheme for different substrate thicknesses. The reduction factor rises when thickness of Si increases and saturates to a value of 4.8 for Si thickness ≥ 20 μm. This clearly indicates the fact that the wavelength-integrated reflectance with and without the light-trapping scheme does not change when Si substrate is thicker than 20 μm as shown in Fig. S1c in Supporting Information. For substrate thicknesses beyond 20 μm, the substrate already has the capability to absorb most of the incident photons but with high reflection loss. In such cases, a simple optimized antireflection coating will serve the purpose of reducing the reflection losses rather than the need for an advanced light management scheme. The Si thickness of 20 μm defines a key transition point for the nanoparticles to display antireflection properties and advanced light management schemes for the underlying Si.

2.2. Light trapping mechanism

To elucidate the light management phenomenon taking place in each layer of the optimized structure, we performed FDTD simulations for varying the angles of incidence and for Transverse Electric (TE) and Transverse Magnetic (TM) polarization of light. The optoelectronic performance of the solar cell should be evaluated for varying angles of incidence, so that non-ideal situations, such as diffused sunlight on a cloudy day and varying incident angles of light depending on the time of the day or the year, could be harnessed efficiently. Since the resonators in the top layer of the optimized bilayer scheme supports excited resonance modes, it is often found that the resonances are polarization sensitive [43,44]. Therefore, for studying the angular dependence of light trapping, we monitored the coupling to individual leaky waveguide modes not only as a function of angle of incidence and excited wavelengths but also for TE and TM polarizations of incidence. Our proposed light-trapping scheme possesses an outstanding broadband and omnidirectional reflectance over a wide range of incident angles. The integrated reflectance of the optimized combination of the nanoparticles on a graphene/Si (20 μm) substrate with varying angles of incidence is shown in Fig. 3**a**. The R_{int} at normal incidence is ~7% and degrades only slightly with increasing angle of incidence. The R_{int} increases by only ~5% as the angle of incidence is increased to 30° and by ~14% at an angle of 50° when compared to reflectance at normal incidence. In contrast, the bare substrate without the light trapping scheme shows ~35% reflectance for normal incidence which gradually increases to ~50% at an angle of incidence of 60°. The R_{int} for varying angles of incidences is the averaged response of two guided modes of excitations at those angles and involves the simulations of the transverse electric (TE) and transverse magnetic (TM) polarized incident light. On analyzing the individual simulations excited by TE and TM mode of incident light separately, it is observed that the integrated reflectance remains unaffected when the light trapping scheme is included as opposed to the substrate without the light-trapping scheme. This is affirmative of the fact that the proposed light-trapping scheme can achieve polarization-independent response for wide angles of incidence [Fig. S2a in Supporting Information]. Fig. 3**b** and **c** show the contour plot of the wavelength-dependent reflectance of the light-trapping scheme on graphene/Si (20 μm) for TE and TM mode of excitation, respectively, with varying angles of incidence. The composite behavior of the two layers helps in suppressing the reflectance from the substrate for both TE and TM modes of excitation for the entire solar spectrum and at all angles of incidence. Fig. S2**b–c** in Supporting Information show the contour plots of wavelength-dependent reflectance when no light-trapping scheme is implemented.

Further, the electric field profiles are obtained for various angles of incidence of light. Fig. 3**d** shows the light trapping mechanism at a wavelength of 680 nm for normal incidence of light. The effects of whispering gallery modes, leaky channel effects and scattering within the substrate are demonstrated for this wavelength by simply scaling the value of the electric field intensity. Spherical silica nanoparticles having refractive index (1.46) higher than the surrounding medium (refractive index of air = 1) can support whispering gallery modes within them [Fig. 3**d (i)**]. Upon entering the nanoparticle, light gets confined within it due to its spherical geometry. Subsequently, angles of incidence for the light striking the internal surface are greater than the critical angle of 43° defined by the silica/air interface. This causes light to travel close to the inner edges of the sphere due to total internal reflections at the silica/air interface. There is also sufficient intra-layer interaction between the particles, allowing for light trapping at higher wavelengths, which is critical for physically thin absorbers [Fig. S3**a-c** in Supporting Information]. This light interaction between dielectric spheres supporting WGM can also be envisaged as a photonic nanojet [45]. These conditions for total internal reflection are supported for both normal angle and oblique angles of incident light. After the light propagates along the surface for one round trip with the same phase, there arises a possibility of formation of constructive interference satisfying the resonance condition of

$$\frac{2\pi \times Radius\ of\ sphere}{Wavelength\ of\ interest} = \frac{l}{Refractive\ index\ of\ sphere} \quad (2)$$

where l is an integer corresponding to the number of round trips for any wavelength [46–48]. According to the Eq. (2), assuming the absence of any leaky mode from the sphere, the silica spheres of the optimized diameter (600 nm) can guide the light in a round trip ~9 times for a wavelength of 300 nm, ~4.5 times for a wavelength of 600 nm and ~2.5 times for a wavelength of 1100 nm. This number of round trips decreases for each wavelength when the size of the nanoparticle

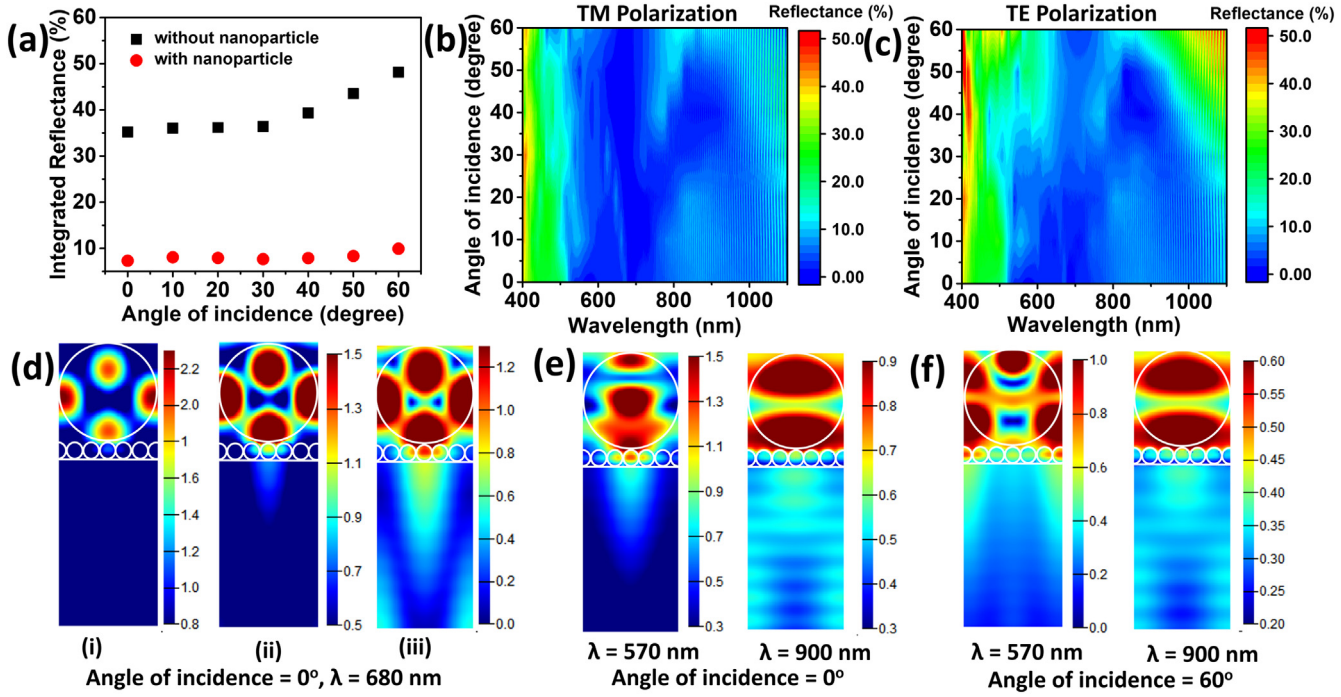

Fig. 3. Light trapping phenomena and the effect of angled incidence. (a) Angle-dependent integrated reflectance of graphene/Si substrate with and without the optimized light trapping structure. Reflectance as a function of wavelength and angle of incidence of light for the graphene/Si substrate with optimized light trapping structure for (b) TM- and (c) TE-polarized light. (d) Electric field profiles of the light-trapping phenomena are shown for an angle of incidence of 0° at 680 nm. Each column of figures corresponds to the advanced light management taking place in the structure itself explaining (i) the formation of whispering gallery modes, (ii) coupling of light from top layer to bottom layer and (iii) light scattering and focusing of light in the active Si absorber. All profiles are for TE polarizations and use a linear color scale representing electric field intensity (V/m) within the light trapping structure and Si for the wavelength of light corresponding to 680 nm. (e) Electric field profiles of the light trapping phenomena for 0° angle of incidence at 570 nm and 900 nm. (f) Electric field profiles of the light trapping phenomena for 60° incidence at 570 nm and 900 nm. The outline of the nanoparticles is marked in white and a Si absorber thickness of 1 μm is depicted.

decreases, underlining their incapacity to support WGMs for the entire solar spectrum. This is evident from the integrated reflectance for the optimizations carried out [Fig. 2**a,** Fig. S1**a–b** in Supporting Information] which show inferior reflectance for lower values of *D:d* ratio for a particular value of '*d*'. This hinders the reduction of the size of the nanoparticles placed in the top layer of our structure. Further, for higher values of *D:d*, the reflectance is found to be asymptotic which is indicative of the presence of WGM in the top nanoparticle layer. However, as the primary objective of the light-trapping scheme is to couple light into the Si substrate, it is not enough to merely trap the light *via* WGMs. The trapped light should be leaked preferentially towards the substrate through suitable leakage channels. This leakage performance of such resonating spheres can be judged by Quality factor, which is defined as

$$Q = \omega_0 \frac{Stored\ energy}{Power\ loss} = \omega_0 \tau \tag{3}$$

where ω_0 represents the angular frequency of the resonator and τ is the time required for the field to decay by a factor of e [49]. Q-factor measures the characteristic time for the exponential decay of the energy stored inside the resonator and is given by the ratio of the total energy stored to the energy dissipated by the resonator. Because of the lossless nature of the dielectric spheres, all-dielectric resonating spheres can support a high Q factor in the solar spectrum. While ideal lossless photonic-bandgap Fabry Perot resonators are capable of Q-factor in the order of 10^5, Q factor reduces to the order of 10^3 for real dielectric materials [50]. FDTD simulation of silica nanoparticles of $D = 600$ nm in air shows a Q factor as high as $\sim 3 \times 10^3$. Whispering gallery modes can leak out from the resonator to the outer free space but at a very low rate due to the low refractive index of the outer medium (air in this case). However, titania nanoparticles offering high refractive index of 2.62 in the bottom layer, leads to the formation of leaky channels for light energy from silica nanoparticles, thus bringing down the Q-factor of the silica nanoparticles to ~78. The low Q factor of the silica nanoparticles in the proposed light trapping configuration causes the incident electric field to decay quickly as compared to an array of similarly sized nanoparticles in air [Fig. S3d in Supporting Information]. Fig. 3**d**(ii) shows the inter-layer coupling of light from the top layer of silica nanoparticles to the bottom layer of titania nanoparticles at an angle of incidence of 0°. The diameter of the bottom layer titania nanoparticles must be such that they can scatter the in-coupled light preferentially into the Si substrate without any significant back scattering. The total scattering efficiency is determined taking into consideration the effect of the size parameter which is given by: [51]

$$Size\ parameter = \frac{2\pi \times Radius\ of\ sphere}{Wavelength\ of\ interest}. \tag{4}$$

The minimum back scattering is obtained for the size parameter ≤ 1 [51]. Small titania nanoparticles ($d \leq 50$ nm) lead to insignificant scattering efficiency resulting in inefficient light trapping inside the active absorber. For larger titania nanoparticles ($d \geq 200$ nm), the scattering efficiency increases significantly, causing a large increase in backward scattering, which is undesirable. An optimum scattering efficiency with negligible back scattering needs a size parameter of 0.6–1 in the solar spectrum [51]. This can be achieved with the use of titania nanoparticles of diameter 100 nm. This also validates the minimum reflection characteristics obtained in the optimization. Fig. 3**d**(iii) shows the scattering of light from the bottom layer into the underlying Si substrate recorded at $\lambda = 680$ nm. The same optical phenomena have been observed at higher angles of incidence as well [Fig. S3e in Supporting Information]. The light trapping mechanisms described at 0° incident angle is also prevalent for an angle of incidence of 60°, demonstrating the omnidirectional property of the light-trapping scheme. Thus, the light-trapping mechanism of the proposed bilayer

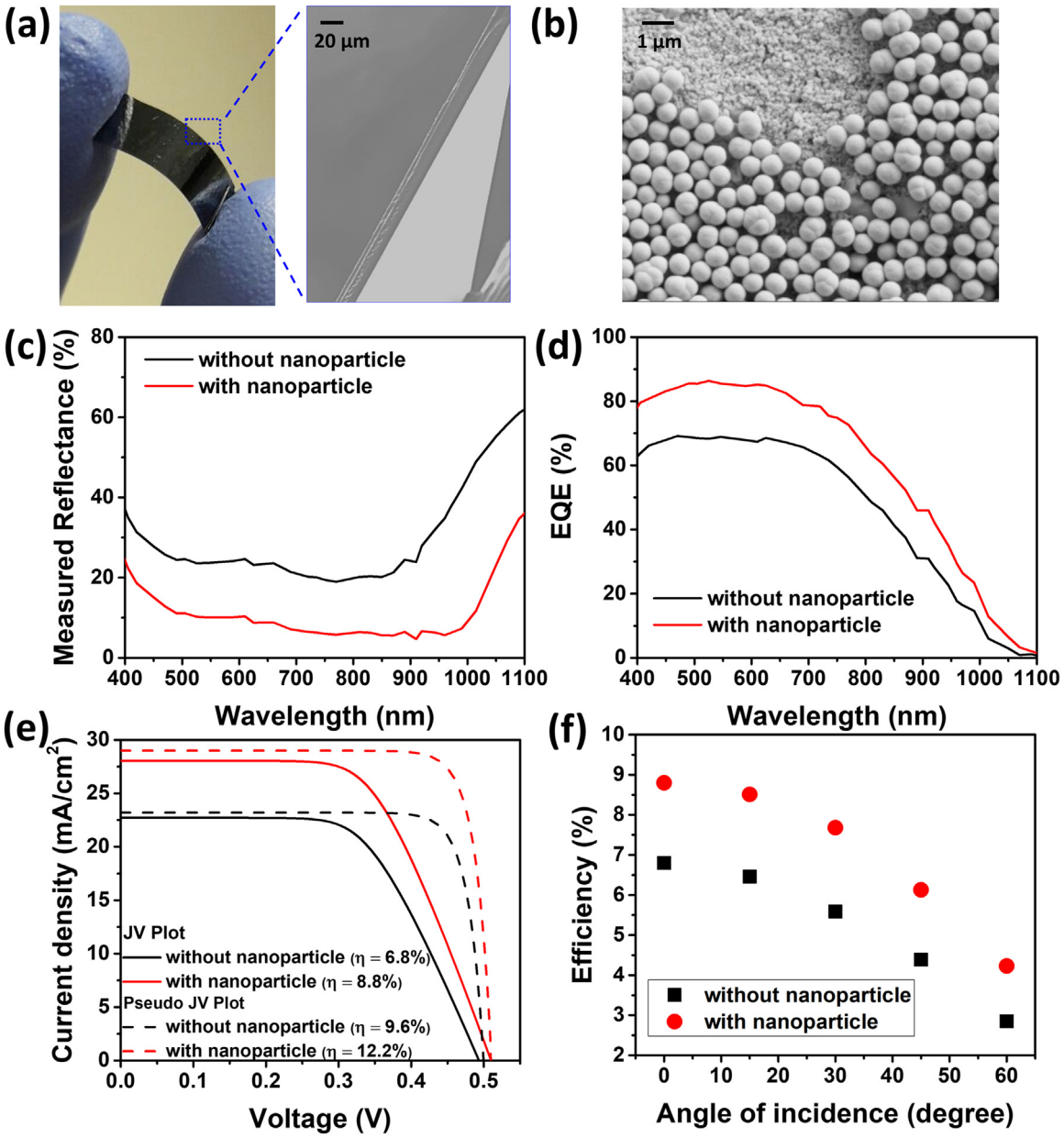

Fig. 4. Characterization of the graphene/Si solar cell with light-trapping scheme. (a) Photograph of a flexible and bendable Si substrate. SEM image confirming the thickness of Si to be 20 µm. (b) SEM image of the bilayer light-trapping scheme with all-dielectric spheres. (c) Experimentally measured reflectance, (d) External quantum efficiency *vs.* wavelength, (e) Current density *vs.* voltage (*J-V*) plot and pseudo *J-V* plot of the final fabricated device and (f) Experimentally measured angle-dependent efficiency of the final fabricated device. The measurements of the device without light-trapping scheme are also shown in the plots for comparison.

scheme exactly mimics the optical behavior of a leaf, exhibiting lensing, waveguiding and scattering of light. The light-trapping effect is not restricted to any particular wavelength. The same effects have been demonstrated also at two other wavelengths of 570 nm and 900 nm for normal and oblique (60°) incidence of light [Fig. 3**e–f**].

2.3. Device characterization

A simple low-cost colloidal spin coating technique is employed to incorporate non-absorbing, all-dielectric spheroidal nanoparticles as the light-trapping scheme on graphene for the fabrication of the flexible ultrathin graphene/Si solar cell. Flexible Si substrate of thickness 20 ± 2 µm was obtained from the n-Si < 100 > substrate [Fig. 4**a**]. A unique methodology of $AuCl_3$-doping followed by spin coating of the silica-titania nanoparticles on as-grown graphene on copper foil is implemented, prior to the wet transfer of graphene on Si. This allows for the composite graphene film to be seamlessly transferred onto the flexible Si substrate with predefined contacts. Fig. 4**b** shows the scanning electron microscope (SEM) image of the bilayer nanoparticles (d ~120 nm, D ~610 nm) on the fabricated device. Solar cell characteristics of the fabricated laminated devices are shown in Fig. 4**c–f**. The measured reflectance for the synthesized nanoparticle combination on graphene/Si solar cell is shown in Fig. 4**c**. The integrated reflectance after incorporating the light trapping scheme is ~10.3%, which is a ~64% reduction in the integrated reflectance compared to a bare graphene/Si surface (R_{int} = ~28.3%). The reflectance of the solar cell without light trapping scheme maintains a broadband response until it starts rising at wavelengths higher than 900 nm. However, the reflectance of the nanoparticle-incorporated solar cells shows an almost flat response up to the wavelength of 1000 nm and then rises slowly at wavelengths beyond that. The reflectance increase at higher wavelengths clearly depicts the signature of a thin Si substrate. The reflection

characteristics of a laminated solar cell with the light-trapping scheme vary marginally from that of a non-laminated device [Fig. S4 in Supporting Information]. The external quantum efficiency (*EQE*) of the device due to the incorporation of the nanoparticles with respect to the bare graphene/Si solar cell is plotted in Fig. 4**d**. The *EQE* increases by ~30% for the entire solar spectrum of wavelengths 400–1100 nm. The reduction in measured reflectance and enhancement in measured *EQE* due to the light-trapping scheme follows the same pattern [Fig. S5**a–b** in Supporting Information]. This clearly explains the advanced light management that is taking place over the entire solar spectrum of 400–1100 nm, predominantly at higher wavelengths. To estimate the current density from EQE measurements, the spectral response is integrated over the solar spectrum 400–1100 nm as per the following equation.

$$J_{sc} = q \int_{400\ \mathrm{nm}}^{1100\ \mathrm{nm}} N_0(\lambda) \times EQE(\lambda) d\lambda \quad (5)$$

where q is the elementary charge and $N_0(\lambda)$ is the number of photons for the incident AM1.5 G solar spectrum. This corresponds to a current density of 20.7 mA/cm^2 and 26.8 mA/cm^2 for the solar cell without and with light trapping scheme respectively. The solar cell *J-V* characteristics are shown in Fig. 4**e**. The graphene/Si solar cell without nanoparticles exhibits an efficiency of 6.8% with J_{sc} of 22.8 mA/cm^2, V_{oc} of 0.49 V, and *FF* of 61%. Series and shunt resistances obtained from the slope of the *J-V* plot at the open circuit voltage and short circuit current point are 5.4 Ω-cm^2 and 100 kΩ-cm^2 respectively. Due to the incorporation of the light-trapping scheme, *PCE* and the J_{sc} reach 8.8% and 28 mA/cm^2 respectively with no change in *FF*. A negligible variation in V_{oc} is obtained from 0.49 V to 0.51 V. The minimal change in V_{oc} (~4%) is attributed to its logarithmic dependence on the current density which makes the variation less pronounced. There is also negligible change in the series and shunt resistances. The increase in the J_{sc} is attributed to the strong coupling of incident light enabled by the bilayer nanoparticle coating. Further, it is observed that the estimated current density values from the EQE measurements are in close agreement with the current densities obtained from the J-V measurement under AM1.5 G solar illumination. The slight under prediction of the short-circuit current from the EQE measurements is because the standard solar spectrum extends into deep UV and far IR which is not considered in the EQE measurement (400–1100 nm) and hence is not in the calculation. Fig. 4**e** also shows the measured pseudo *J-V* characteristics of the solar cells. The pseudo *J-V* curves show little difference compared to the actual *J-V* plot besides an increased *FF*. The current (J_{sc}) and voltage (V_{oc}) points have negligible change. The *FF* of the pseudo *J-V* plot comes around 84% as compared to 61% obtained from the real *J-V* plot. As observed from the pattern of the plots in the figure, we can conclude that the cell is not significantly impacted by shunting, and that the series resistance is the major cause of *FF* loss. To evaluate the omnidirectional performance of our devices, we have compared the device performance for different angles of incidence from 0° to 60°. Fig. 4**f** shows the angle-dependent efficiencies of the fabricated device before and after incorporating the light trapping structures. It is observed that the efficiency decreases for increased angles of incidence in both the cases with or without nanoparticles. This is due to the cosine effect which results in reduction of incident radiation by the cosine of the angle between the solar radiation and a surface normal. To estimate the actual current density generated by the solar cell nullifying the impact of the reduced incident flux due to the cosine effect, a normalized value of current density as a function of angles of incidence for the solar cell with or without light trapping structure is presented in supporting information [Fig. S5c in Supporting Information]. It is observed that the bio-inspired solar cell shows a minimal deviation (relative change of ~3%) of the current density over the wide angles of incidence (0–60°) as compared to the bare graphene/Si solar cell where the variation is 16% for the minimum (0°) and maximum (60°) angle of incidence. These observations confirm the role of the bilayer nanoparticle light-trapping scheme as an omnidirectional anti-reflection layer. Further, the obtained *PCE* in a substrate thickness of 20 μm translates to enormous material cost savings resulting in the highest Watt/gram Si utilization of 1.89 as compared to other reported works [Table S1 in Supporting Information]. This also implies that only 0.53 g of active material is needed to produce power output of 1 W from such devices. A table showing the device performance parameters of a number of graphene/silicon solar cells having the optimized light trapping structure is shown in Supporting Information [Table S2] with the champion solar cell having an efficiency of 8.8%. As seen from the table, the fabrication process flow is repeatable and reproducible; and the PCE values are highly consistent with a tight PCE distribution (~3% relative change). To investigate the stability in the reported efficiency of the solar cell and aging effect of the solar cell, the cell is examined and is found to show stable performance even after 4 months [Fig. S6 in Supporting Information] retaining ~96% of the initial *PCE* value without deterioration of the key photovoltaic properties such as J_{sc}, V_{oc}, and *FF*. To demonstrate the flexibility and reliability of the fabricated solar cell with light trapping scheme, the graphene/Si solar cell with the light trapping scheme has been subjected to bending tests with different bending radii and cycles. Solar *J-V* characteristics are measured after certain intervals (10th, 50th, 100th, 300th, 500th, 700th and 1000th cycle) for three different bending radii of 20 mm, 10 mm and 3 mm by repeating the bending-recovering cycles. A photograph of the bending test is shown in Fig. 5**a.** The effect of repeated bending on device parameters and PCE as a function of bending cycles is presented in Fig. 5**b** and **c** respectively. V_{oc} remains almost unchanged (from 0.51 V to 0.50 V) with a minimal variation of J_{sc} between 26 mA/cm^2 to 28 mA/cm^2. As a result, the *PCE* is also found to be within the range of 8.8–8.3% for bend radius of 20 mm, 10 mm and 3 mm. This is indicative of the fact that the device is capable of retaining ~95% of the its original performance even after bending it over 10^3 bending cycles of varying radii. The results demonstrate the excellent flexibility as well as high durability of the fabricated solar cells.

3. Conclusions

In summary, we fabricated a graphene/Si Schottky junction solar cell on planar 20 μm ultrathin Si substrate, having an efficiency of ~9%, using a leaf-inspired biomimetic light trapping scheme. The scheme involves the use of two optically tuned lossless nanoparticle layers. The nanoparticles in the top silica layer behave as low-Q whispering gallery mode resonators, which confine light and direct it into the bottom titania layer through the strong energy leakage channels. The bottom layer subsequently scatters the coupled light into the high index Si absorber. Using FDTD simulation, it is found that the light-trapping capability is maximized when the particle diameter of the top layer is within 600 nm, and a ratio of 6:1 is maintained between the diameters of the top and bottom layers of nanoparticles. A 30% enhancement in the *EQE* is achieved due to the nanoparticle coating. The measured *PCE* of the nanoparticle-coated graphene/Si solar cells for varying angles of incidence confirms the omnidirectional behavior of the light-trapping scheme, enabled by the intra-layer and inter-layer nanoparticle interactions. The all-dielectric light-trapping scheme does not increase surface recombination, establishing its advantages over conventional techniques, such as nanostructuring of active absorber substrate. The work also demonstrates that graphene may be seamlessly integrated into the technology roadmap of monocrystalline Si solar cells with simple low-cost light trapping schemes. Further, the fabricated solar cells exhibit highly reliable behavior for 10^3 bending cycles for bend radii of 20 mm, 10 mm and 3 mm. This validates the capability of the devices as future solar cell technologies since next generation solar cells should be low-cost, flexible and can be fabricated by roll-to-roll processing.

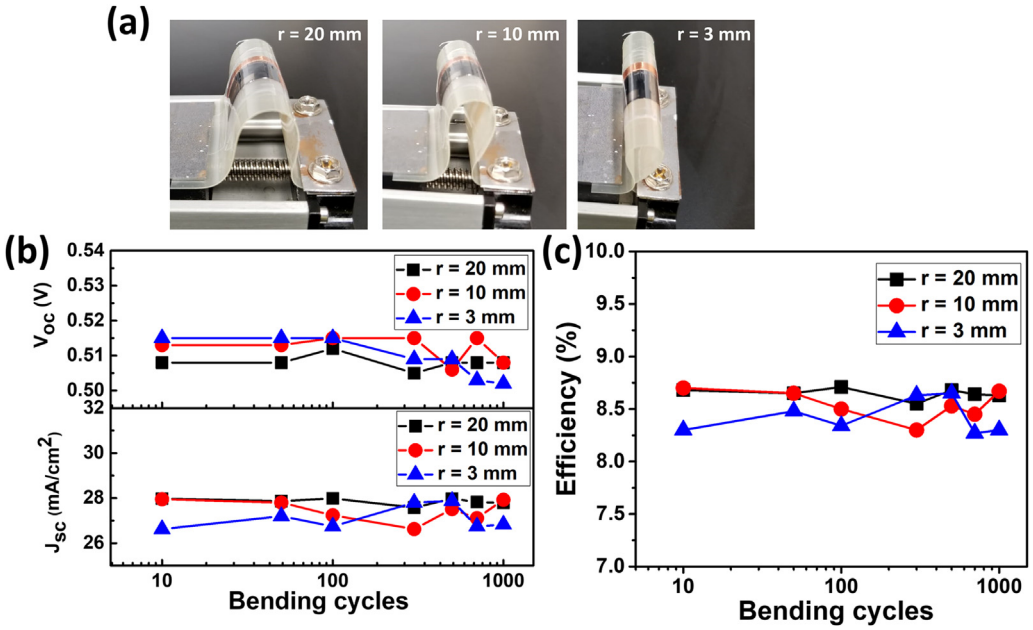

Fig. 5. Bending analysis of the graphene/Si solar cell with light trapping structure. (a) Photograph of the solar cell under different bending conditions with various radii of curvature. Variation of (b) open circuit voltage (V_{oc})and short circuit current density (J_{sc}) and (c) efficiency with increasing bending cycles.

4. Material and methods

4.1. Optical simulation

A three-dimensional full wave FDTD simulation (Lumerical Solution, Inc.) is used to optimize the light-trapping scheme for the graphene/Si interface. We have considered bilayer graphene on planar Si. The material properties of Si are taken from the database of Palik [52] in the FDTD simulator and constant refractive indices are used for SiO_2 (n = 1.46) and TiO_2 (n = 2.62). A 2D rectangle sheet is used to model the graphene sheet based on the surface conductivity of graphene [53]. To simulate a bilayer graphene, graphene model with conductivity scaling of 2 is considered [54]. Simulation box is defined across the size of a unit cell with symmetric/antisymmetric boundaries in the lateral direction and perfectly matched layers in the vertical direction. Aluminium back reflector is used to define the bottom boundary condition. A planar wave source having the spectrum range of 400–1000 nm is considered for simulation. Power monitors are placed above the source to capture the wavelength dependent reflection. Moreover, the structure is analyzed by oblique incident plane waves using Broadband Fixed Angle Source Technique sources to simulate its response for varying angles of incidence. Simulations are performed for both TM and TE polarized light and are averaged out to obtain the total reflection loss for various angles of incidence. Electric field profiles for each wavelength are recorded with frequency domain field profile monitors. For simulating the Q-factor for the structure, time monitors are placed at different locations in the simulation box to isolate the resonant peaks. The quality factor is quantified from the slope of the envelope of the decaying signal by the formula [54]

$$Q = -\frac{2\pi \times resonant\ frequency \times log_{10}^{e}}{2\times Slope\ of\ the\ timesignal\ decay}$$

4.2. Nanoparticle synthesis

Both silica and titania nanoparticles are synthesized by the well-known Stober method by the hydrolysis and subsequent condensation of alkyl silicate (Tetra Ethyl Ortho Silicate) [55,56] and alkyl titanate (Ttianium Isopropoxide) [57] respectively at room temperature. Ammonium hydroxide is added as a catalyst in the reaction to maintain the desired alkalinity of both the solution. While silica nanoparticles are prepared in a medium of ethanol and water at a stirring speed of 1000 rpm, titania nanoparticles are prepared only in water medium at 2000 rpm. Finally, the prepared solution is centrifuged to obtain the final colloidal solution. Concentration of the reaction mixture, stirring speed and time of the reaction are optimized to obtain the desired diameter of nanoparticles. The synthesized nanoparticles are spin coated on doped graphene to form a monolayer hexagonal close packing array.

4.3. Device fabrication

To fabricate the graphene/Si Schottky junction Schottky type solar cell, n-type Czochralski Si wafers (< 100 > , 1–20 Ωcm, 180–200 μm thick) is immersed into 30 wt% KOH solutions heated at 90 °C. By controlling the etching duration time, ultrathin Si substrates 20 μm thick are obtained. The wafers are cleaned in a 10% aqueous HF solution at room temperature to get rid of native oxide from the surface. Aluminium (100 nm) is deposited by electron beam evaporation to form the back contact of the solar cell. An interfacial oxide layer of Al_2O_3 (1 nm) is deposited by atomic layer deposition at 250 °C using tri-methyl Al (TMA) as Al precursor and H_2O as oxygen precursor using an atomic layer deposition system (Savannah, Ultratech/CNT). A masked deposition of the insulating layer of SiO_2 (300 nm) is performed in Plasma-enhanced chemical vapor deposition system (PlasmaTherm 790) at a temperature of 250 °C. This is followed by masked deposition of nickel to form the top electrode. Bilayer graphene grown on copper foil (purchased from ACS Materials Inc.) [58] was transferred onto the Si substrate by polymethyl methacrylate (PMMA) assisted wet transfer process [59]. Graphene was p-doped and spin coated with the nanoparticles prior to PMMA coating. Doping was performed by spin-casting $AuCl_3$ dissolved (20 mM) in nitromethane at 2000 rpm for 1 min. Spin coating of titania nanoparticles followed by silica nanoparticles are performed to obtain a uniform coverage all over the doped graphene. The fabricated graphene/Si devices are finally annealed in a tube furnace with 1:9::H_2:N_2 at 400 °C for 3 h to remove the PMMA and for better adhesion of graphene with the substrate. Prior to lamination, long strips of copper tapes with adhesive lining was affixed on to the

front and back contacts of the fabricated solar cell. For lamination, the front side of the solar cell is placed face down onto a 25 μm thin Polyethylene terephthalate (PET) sheet. The self-seal laminating layers with adhesive lining are placed evenly onto the back of solar cell while applying downward pressure. The entire device is firmly pressed subsequently to smooth and seal the edges of the lamination without any trapped air bubble.

4.4. Material and device characterization

Solar *J-V* characteristics are measured under one sun illumination using a Keysight B1500A Semiconductor Device Analyzer. Solar *J-V* characteristics are also measured by varying the incident angle of light between 0° and 60°. Pseudo J-V characteristics are measured by Sinton Instruments Suns-Voc standalone measurement set up. Experiments on bending mechanism of the ultrathin flexible solar cells are performed by a simplified motorized motion controller *via* computer peripheral. External quantum efficiency and reflectance measurements are obtained with a Tau Science FlashQE coupled with an integrated sphere, and both are measured for the wavelength range of 400–1100 nm. SEM images are taken in Zeiss ULTRA-55 FEG SEM.

Acknowledgements

This work was supported by UCF startup fund for T.R., number 20080746.

Conflict of interest

The authors declare no conflict of interest.

Appendix A. Supporting information

Supplementary data associated with this article can be found in the online version at doi:10.1016/j.nanoen.2018.12.072.

References

[1] P. Sonntag, N. Preissler, M. Bokalič, M. Trahms, J. Haschke, R. Schlatmann, M. Topič, B. Rech, D. Amkreutz, Silicon solar cells on glass with power conversion efficiency above 13% at thickness below 15 μm, Sci. Rep. 7 (2017) 873, https://doi.org/10.1038/s41598-017-00988-x.

[2] R. Islam, K. Saraswat, Limitation of optical enhancement in ultra-thin solar cells imposed by contact selectivity, Sci. Rep. 8 (2018) 8863, https://doi.org/10.1038/s41598-018-27155-0.

[3] A.B. Roy, A. Dhar, M. Choudhuri, S. Das, S.M. Hossain, A. Kundu, Black silicon solar cell: analysis optimization and evolution towards a thinner and flexible future, Nanotechnology 27 (2016) 305302, https://doi.org/10.1088/0957-4484/27/30/305302.

[4] X. Li, M. Mariano, L. McMillon-Brown, J.S. Huang, M.Y. Sfeir, M.A. Reed, Y. Jung, A.D. Taylor, Charge transfer from carbon nanotubes to silicon in flexible carbon nanotube/silicon solar cells, Small 13 (2017) 1702387, https://doi.org/10.1002/smll.201702387.

[5] H.P. Wang, J.H. He, Toward highly efficient nanostructured solar cells using concurrent electrical and optical design, Adv. Energy Mater. 7 (2017) 1602385, https://doi.org/10.1002/aenm.201602385.

[6] H.A. Atwater, A. Polman, Plasmonics for improved photovoltaic devices, Nat. Mater. 9 (2010) 205, https://doi.org/10.1038/nmat2629.

[7] G.-J. Lin, H.-P. Wang, D.-H. Lien, P.-H. Fu, H.-C. Chang, C.-H. Ho, C.-A. Lin, K.-Y. Lai, J.-H. He, A broadband and omnidirectional light-harvesting scheme employing nanospheres on Si solar cells, Nano Energy 6 (2014) 36–43, https://doi.org/10.1016/j.nanoen.2014.03.004.

[8] B. Bhushan, Biomimetics: lessons from nature–an overview, Philos. Trans. A Math. Phys. Eng. Sci. (2009), https://doi.org/10.1098/rsta.2009.0011.

[9] R.J. Martín-Palma, A. Lakhtakia, Progress on bioinspired, biomimetic, and bioreplication routes to harvest solar energy, Appl. Phys. Rev. 4 (2017) 021103, https://doi.org/10.1063/1.4981792.

[10] A. Rahman, A. Ashraf, H. Xin, X. Tong, P. Sutter, M.D. Eisaman, C.T. Black, Sub-50-nm self-assembled nanotextures for enhanced broadband antireflection in silicon solar cells, Nat. Commun. 6 (2015) 5963, https://doi.org/10.1038/ncomms6963.

[11] S.A. Boden, D.M. Bagnall, Optimization of moth-eye antireflection schemes for silicon solar cells, Prog. Photovolt.: Res. Appl. 18 (2010) 195–203, https://doi.org/10.1002/pip.951.

[12] R. Dewan, S. Fischer, V.B. Meyer-Rochow, Y. Özdemir, S. Hamraz, D. Knipp, Studying nanostructured nipple arrays of moth eye facets helps to design better thin film solar cells, Bioinspir. Biomim. 7 (2011) 016003, https://doi.org/10.1088/1748-3182/7/1/016003.

[13] T. Feng, D. Xie, Y. Lin, Y. Zang, T. Ren, R. Song, H. Zhao, H. Tian, X. Li, H. Zhu, Graphene based Schottky junction solar cells on patterned silicon-pillar-array substrate, Appl. Phys. Lett. 99 (2011) 233505, https://doi.org/10.1063/1.3665404.

[14] Z. Arefinia, A. Asgari, A new modeling approach for graphene based silicon nanowire Schottky junction solar cells, J. Renew. Sustain. Energy 6 (2014) 043132, https://doi.org/10.1063/1.4893433.

[15] S.L. Diedenhofen, G. Vecchi, R.E. Algra, A. Hartsuiker, O.L. Muskens, G. Immink, E.P. Bakkers, W.L. Vos, J.G. Rivas, Broad-band and omnidirectional antireflection coatings based on semiconductor nanorods, Adv. Mater. 21 (2009) 973–978, https://doi.org/10.1002/adma.200802767.

[16] H.-P. Wang, K.-T. Tsai, K.-Y. Lai, T.-C. Wei, Y.-L. Wang, J.-H. He, Periodic Si nanopillar arrays by anodic aluminum oxide template and catalytic etching for broadband and omnidirectional light harvesting, Opt. Express 20 (2012) A94–A103, https://doi.org/10.1364/OE.20.000A94.

[17] Y.-C. Chao, C.-Y. Chen, C.-A. Lin, J.-H. He, Light scattering by nanostructured antireflection coatings, Energy Environ. Sci. 4 (2011) 3436–3441, https://doi.org/10.1039/C0EE00636J.

[18] A.V. Ruban, Plants in light, Commun. Integr. Biol. 2 (2009) 50–55, https://doi.org/10.4161/cib.2.1.7504.

[19] A.V. Ruban, Evolution under the sun: optimizing light harvesting in photosynthesis, J. Exp. Bot. 66 (2014) 7–23, https://doi.org/10.1093/jxb/eru400.

[20] J. Grandidier, D.M. Callahan, J.N. Munday, H.A. Atwater, Light absorption enhancement in thin-film solar cells using whispering gallery modes in dielectric nanospheres, Adv. Mater. 23 (2011) 1272–1276, https://doi.org/10.1002/adma.201004393.

[21] Z. Yang, P. Gao, C. Zhang, X. Li, J. Ye, Scattering effect of the high-index dielectric nanospheres for high performance hydrogenated amorphous silicon thin-film solar cells, Sci. Rep. 6 (2016), https://doi.org/10.1038/srep30503.

[22] Y. Yao, J. Yao, V.K. Narasimhan, Z. Ruan, C. Xie, S. Fan, Y. Cui, Broadband light management using low-Q whispering gallery modes in spherical nanoshells, Nat. Commun. 3 (2012) 664, https://doi.org/10.1038/ncomms1664.

[23] D. Parrain, C. Baker, G. Wang, B. Guha, E.G. Santos, A. Lemaitre, P. Senellart, G. Leo, S. Ducci, I. Favero, Origin of optical losses in gallium arsenide disk whispering gallery resonators, Opt. Express 23 (2015) 19656–19672, https://doi.org/10.1364/OE.23.019656.

[24] M. Gomilšek, Whispering gallery modes, Univ Ljubl Ljubl Semin, 2011.

[25] J. Zhu, Ş.K. Özdemir, H. Yilmaz, B. Peng, M. Dong, M. Tomes, T. Carmon, L. Yang, Interfacing whispering-gallery microresonators and free space light with cavity enhanced Rayleigh scattering, Sci. Rep. 4 (2014) 6396, https://doi.org/10.1038/srep06396.

[26] T.K. Das, P. Ilaiyaraja, C. Sudakar, Whispering gallery mode assisted enhancement in the power conversion efficiency of DSSC and QDSSC devices using TiO2 microsphere photoanodes, ACS Appl. Energy Mater. 1 (2018) 765–774, https://doi.org/10.1021/acsaem.7b00207.

[27] S. Das, D. Pandey, J. Thomas, T. Roy, The role of graphene and other 2D materials in solar photovoltaics, Adv. Mater. (2018), https://doi.org/10.1002/adma.201802722.

[28] X. Yu, K. Sivula, Toward large-area solar energy conversion with semiconducting 2D transition metal dichalcogenides, ACS Energy Lett. 1 (2016) 315–322, https://doi.org/10.1021/acsenergylett.6b00114.

[29] J.Y. Lee, J.-H. Shin, G.-H. Lee, C.-H. Lee, Two-dimensional semiconductor optoelectronics based on van der Waals Heterostructures, Nanomaterials 6 (2016) 193, https://doi.org/10.3390/nano6110193.

[30] W. Tang, S. Rassay, N. Ravindra, Electronic & optical properties of transition-metal dichalcogenides, Madridge J. Nano Technol. 2 (2017) 59–65, https://doi.org/10.18689/mjnn.2017-110.

[31] S. Ju, B. Liang, J.-Z. Wang, Y. Shi, S.-L. Li, Graphene/silicon Schottky solar cells: technical strategies for performance optimization, Opt. Commun. (2018), https://doi.org/10.1016/j.optcom.2018.02.033 (https://doi.org/10.1016/j.optcom.2018.02.033).

[32] Y. Ye, L. Dai, Graphene-based Schottky junction solar cells, J. Mater. Chem. 22 (2012) 24224–24229, https://doi.org/10.1039/C2JM33809B.

[33] A. Louwen, W. Van Sark, R. Schropp, A. Faaij, A cost roadmap for silicon heterojunction solar cells, Sol. Energy Mater. Sol. Cells 147 (2016) 295–314, https://doi.org/10.1016/j.solmat.2015.12.026.

[34] Y. Song, X. Li, C. Mackin, X. Zhang, W. Fang, T. s. Palacios, H. Zhu, J. Kong, Role of interfacial oxide in high-efficiency graphene–silicon Schottky barrier solar cells, Nano Lett. 15 (2015) 2104–2110, https://doi.org/10.1063/1.498188010.1021/nl505011f.

[35] J. Ahn, H. Chou, S.K. Banerjee, Graphene-Al2O3-silicon heterojunction solar cells on flexible silicon substrates, J. Appl. Phys. 121 (2017) 163105, https://doi.org/10.1063/1.4981880.

[36] T.C. Vogelman, J.N. Nishio, W.K. Smith, Leaves and light capture: light propagation and gradients of carbon fixation within leaves, Trends Plant Sci. 1 (1996) 65–70, https://doi.org/10.1016/S1360-1385(96)80031-8.

[37] K. Ma, F. Baret, P. Barroy, L. Bousquet, editors. A leaf optical properties model accounting for differences between the two faces, in: Proceedings of the 10th International Symposium on Physical Measurements and Signatures in Remote Sensing, 2007 ISPMSRS07, Citeseer, 2007.

[38] Y. Song, X. Li, C. Mackin, X. Zhang, W. Fang, T. Palacios, H. Zhu, J. Kong, Role of interfacial oxide in high-efficiency graphene − silicon schottky barrier solar cells, Nano Lett. 15 (2015) 2104–2110, https://doi.org/10.1021/nl505011f.

[39] W. Zhang, F. Wang, K.O. Davis, K. Jiang, W.V. Schoenfeld, J.P. Looney, editors.

Interfacial structure and passivation properties of Al_2O_3 on silicon, in: Proceedings of the IEEE 44th Photovoltaic Specialist Conference (PVSC); 2017: IEEE, 2017.
[40] J.W. Suk, A. Kitt, C.W. Magnuson, Y. Hao, S. Ahmed, J. An, A.K. Swan, B.B. Goldberg, R.S. Ruoff, Transfer of CVD-grown monolayer graphene onto arbitrary substrates, ACS Nano 5 (2011) 6916–6924, https://doi.org/10.1021/nn201207c.
[41] A. Alnuaimi, I. Almansouri, I. Saadat, A. Nayfeh, Interface engineering of graphene–silicon Schottky junction solar cells with an Al2O3 interfacial layer grown by atomic layer deposition, RSC Adv. 8 (2018) 10593–10597, https://doi.org/10.1016/j.carbon.2018.02.042.
[42] M.A. Rehman, I. Akhtar, W. Choi, K. Akbar, A. Farooq, S. Hussain, M.A. Shehzad, S.-H. Chun, J. Jung, Y. Seo, Influence of an Al2O3 interlayer in a directly grown graphene-silicon Schottky junction solar cell, Carbon 132 (2018) 157–164, https://doi.org/10.1016/j.carbon.2018.02.042.
[43] M.N.M. Nasir, S.B. Gorajoobi, G.S. Murugan, M.N. Zervas, editors. Polarisation effects in optical microresonators, in: Proceedings of the Photonics Conference (IPC), 2015: IEEE, 2015.
[44] Y. Han, J.-A. Huang, X.-Y. Liu, X.-J. Zhang, J.-X. Shi, C.-C. Yan, Polarization-independent broadband plasmonic absorber based on a silicon-nanowire array decorated by gold nanoparticles at the optical regime, Opt. Express 24 (2016) 9178–9186, https://doi.org/10.1364/OE.24.009178.
[45] Z. Chen, A. Taflove, V. Backman, Highly efficient optical coupling and transport phenomena in chains of dielectric microspheres, Opt. Lett. 31 (2006) 389–391, https://doi.org/10.1364/OL.31.000389.
[46] A. Chiasera, Y. Dumeige, P. Feron, M. Ferrari, Y. Jestin, G. Nunzi Conti, S. Pelli, S. Soria, G.C. Righini, Spherical whispering-gallery-mode microresonators, Laser Photon Rev. 4 (2010) 457–482, https://doi.org/10.1002/lpor.200910016.
[47] G. Righini, Y. Dumeige, P. Féron, M. Ferrari, G. Nunzi Conti, D. Ristic, S. Soria, Whispering gallery mode microresonators: fundamentals and applications, Riv. Nuovo Cim. 34 (2011) 435–488, https://doi.org/10.1393/ncr/i2011-10067-2.
[48] D.V. Strekalov, C. Marquardt, A.B. Matsko, H.G. Schwefel, G. Leuchs, Nonlinear and quantum optics with whispering gallery resonators, J. Opt. 18 (2016) 123002, https://doi.org/10.1088/2040-8978/18/12/123002.
[49] I. Kandas, B. Zhang, C. Daengngam, I. Ashry, C.-Y. Jao, B. Peng, S.K. Ozdemir, H.D. Robinson, J.R. Heflin, L. Yang, High quality factor silica microspheres functionalized with self-assembled nanomaterials, Opt. Express 21 (2013) 20601–20610, https://doi.org/10.1364/OE.21.020601.
[50] J.H. Wu, L.K. Ang, A.Q. Liu, H.G. Teo, C. Lu, Tunable high-Q photonic-bandgap Fabry-Perot resonator, JOSA B 22 (2005) 1770–1777, https://doi.org/10.1364/JOSAB.22.001770.
[51] B.S. Luk'yanchuk, N.V. Voshchinnikov, R. Paniagua-Domínguez, A.I. Kuznetsov, Optimum forward light scattering by spherical and spheroidal dielectric nanoparticles with high refractive index, ACS Photonics 2 (2015) 993–999, https://doi.org/10.1021/acsphotonics.5b00261.
[52] E. Palik, G. Ghosh, Handbook of Optical Constants of Solids, Academic, New York, 1985.
[53] A. Andryieuski, A.V. Lavrinenko, Graphene metamaterials based tunable terahertz absorber: effective surface conductivity approach, Opt. Express 21 (2013) 9144–9155, https://doi.org/10.1364/OE.21.009144.
[54] Available from: ⟨https://kb.lumerical.com/⟩.
[55] S. Das, C. Banerjee, A. Kundu, P. Dey, H. Saha, S.K. Datta, Silica nanoparticles on front glass for efficiency enhancement in superstrate-type amorphous silicon solar cells, J. Phys. D: Appl. Phys. 46 (2013) 415102, https://doi.org/10.1088/0022-3727/46/41/415102.
[56] W. Stöber, A. Fink, E. Bohn, Controlled growth of monodisperse silica spheres in the micron size range, J. Colloid Interface Sci. 26 (1968) 62–69, https://doi.org/10.1016/0021-9797(68)90272-5.
[57] D. Fattakhova-Rohlfing, A. Zaleska, T. Bein, Three-dimensional titanium dioxide nanomaterials, Chem. Rev. 114 (2014) 9487–9558, https://doi.org/10.1021/cr500201c.
[58] ⟨https://www.acsmaterial.com/⟩.
[59] J. Chan, A. Venugopal, A. Pirkle, S. McDonnell, D. Hinojos, C.W. Magnuson, R.S. Ruoff, L. Colombo, R.M. Wallace, E.M. Vogel, Reducing extrinsic performance-limiting factors in graphene grown by chemical vapor deposition, ACS Nano 6 (2012) 3224–3229, https://doi.org/10.1021/nn300107f.